**Magnesium Technology 2012**
*Edited by: Suveen N. Mathaudhu, Wim H. Sillekens, Neale R. Neelameggham, and Norbert Hort*
***TMS (The Minerals, Metals & Materials Society), 2012***

# ATOMS-TO-GRAINS CORROSION MODELING FOR MAGNESIUM ALLOYS

Hyunwook Kwak[1], Jie Xiao, and Santanu Chaudhuri[1*]

[1]ISP/Applied Sciences Laboratory, Washington State University, WA 99210-1495

Keywords: Corrosion Protection, First-Principles Calculations, MgO, Rare-Earth Doping

**Abstract**

Development of new Mg-alloys needs greater efforts in systematic evaluation of corrosion protection methods under service environments. A deeper understanding of microscale and nanoscale metallurgy is needed to slow down corrosion. Results from our multiscale modeling effort will be presented to demonstrate the power of first-principle theories in predicting the composition-dependent kinetics of corrosion reactions. Our recent results show that the corrosion prevention properties of Mg-alloys can be significantly enhanced by doping rare-earth elements such as Cerium that protects the oxide layer from rapid hydrolysis. Furthermore, we are developing kinetic Monte Carlo and finite-element analysis (FEA) based models to extend the predictions from the atomic length scales to nano- and microscale models that will include grains and alloy microstructure. The potential for incorporating mechanical and corrosion performance in continuum length scale combined with the insights from first-principles based surface chemical models can have powerful impact on the development of Mg-alloys.

## Introduction

Our initial multiscale simulation results on Mg alloys indicate that corrosion mechanisms in Mg alloys are unique.[1] Therefore it is important that corrosion prevention strategies need to include consideration for specific mechanistic pathways to prevent failures and find mature alloys for structural applications. From optimizing composition of promising alloys, increasing the stability of the oxide layer, and obtaining a uniform microstructure through carefully controlled processing conditions, all play a part in reducing corrosion vulnerabilities. Our simulation effort is geared towards understanding different galvanic and dissolution processes in hot and humid environments. Some theoretical development will be needed to address the role of electrochemical field inside the pits at the intermetallic particle boundaries. In alloys such as AZ31, AZ80 and AZ91D, there are different phases of intermetallic precipitates that are formed in the alloy matrix. Intermetallic impurities or inclusions such as $Al_2Mn$, $Mg_{17}Al_{12}$ etc. have the potential to act as a cathode and expedite the oxide film and alloy etching where the Mg-alloy matrix acts as anode. In this current work, we will discuss stability of MgO film without intermetallic impurities across different length scales and identify the links between elemental doping of the MgO surface and the correlation with metal loss from atomistic to microscale.

Figure 1 illustrates the framework we are developing for understanding and prescribing predictive pathways to slow-down corrosion. It consists of four layers of modeling blocks, which are bi-directionally coupled and closely connected with a block of experimental data. At the bottom layer, first-principles-based calculations are responsible for generating thermodynamic information, such as Gibbs free energy of activation for a chemical or electrochemical reaction. This information is critical for kinetic Monte Carlo and molecular dynamics (kMC/MD) simulation of corrosion phenomena on and nearby the metal-electrolyte interface at nanoscale, e.g., oxide layer formation, ion adsorption, desorption, and diffusion through oxide/hydroxide layer, and metal dissolution, etc. On the other hand, reaction kinetics derived from first-principles calculation and kMC/MD simulation can be fed into an upper layer. At this layer, finite element models describe the growth of a single pit, where metal microstructure, pit surface morphology, and corrosion environment are systematically taken into account. Detailed investigation on the growth of a single pit will eventually lead to a successful study of the evolution of an ensemble of pits at macroscopic time and length scales by using the damage function analysis (DFA) method. Finally, corrosion performance evaluation (such as life time quantification) will be conducted at the top layer.

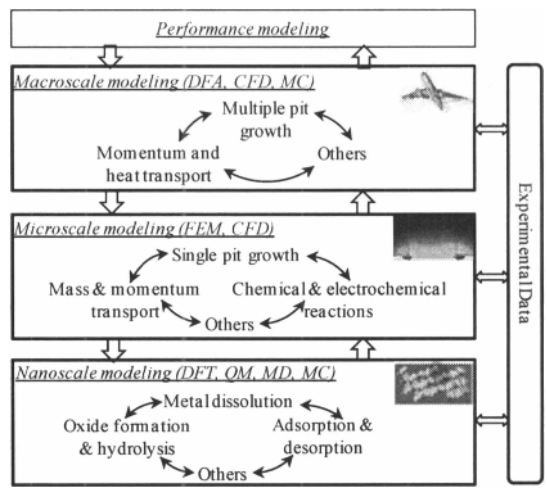


Figure 1. Multiscale modeling framework of corrosion

Oxide film on top of Mg alloys plays an important role on the corrosion protection of pure magnesium and Mg alloys. Presence of alloying compounds in the alloy is also important for the oxide films because the alloying species can transport to the metal surface and alter the composition of the oxide film. This observation is backed by numerous previous work where traces of excessive alloying compounds were detected at the protective films on top of Y-enriched and Ce-enriched Mg alloy systems. The primary emphasis of first-principles based *corrosion modeling effort* is to develop understanding of interfacial reactions as a function of surface composition of alloys under humid and corrosive conditions. Mg-alloys are particularly vulnerable in

humid environment due to hydrolysis of MgO layers to $Mg()H)_2$ as shown in figure 2 . Once this barrier layer is damaged, galvanic processes leads to rapid loss of Mg due to its position in the electrochemical series.

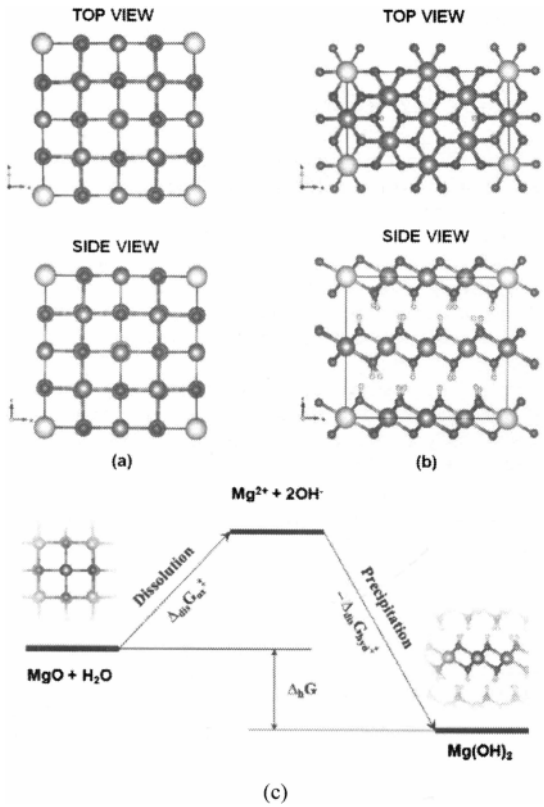


Figure 2 (a) The unit cell of MgO, and (b) $Mg(OH)_2$ from top and side-view of atomic arrangements. (c) We calculate the thermodynamics from a two-step reaction model for the hydroxylation of the oxide films on Mg alloy.

## Methods

Thermochemical properties from first principles

The key to our thermodynamic description of the hydroxylation process for the doped oxides is the use of first-principles methods to calculate the overall change in thermochemical potential during the following hydroxylation process,

$$\mathrm{MgO(periclase)} + \mathrm{H_2O_{(l)}} \longrightarrow \mathrm{Mg(OH)_2(brucite)} \qquad (1)$$

For oxide films in contact with aqueous solution at room temperature, we consider a system that is exposed to a solution reservoir in which temperature, pressure, and activities of solute species are kept constant at standard condition. The appropriate thermodynamic potential to describe such a system is Gibbs free energy. Based on the definition of Gibbs free energy (G = U – TS + pV), the temperature-dependent free energy of a solid can be approximated as follows,

$$G = U_{\mathrm{elec}} + F_{\mathrm{vib}}(T) + pV \qquad (2)$$

The first term indicates the electronic total energy that corresponds to the ground state energy of a system at 0 K. The second term corresponds to the free energy contribution from the vibrational excitation of solids $\left(F_{\mathrm{vib}}(T) = U_{\mathrm{vib}}(T) - TS_{\mathrm{vib}}(T)\right)$. For gas phase substances, similar expression can be given,

$$G \simeq U_{\mathrm{elec}} + F_{\mathrm{trans}}(T) + F_{\mathrm{rot}}(T) + F_{\mathrm{vib}}(T) + pV \qquad (3)$$

where the translational and the rotational free energy of a gas molecule ( $F_{\mathrm{trans}} + F_{\mathrm{rot}}$ ) is also considered. From our methodology, the first three terms of Eqn. (2) are calculated from electronic structure and phonon frequency calculations based on DFT. Change in the $pV$ term is neglected for solids since they are at least several orders of magnitude smaller than the change in the internal energy at standard temperature and pressure condition.

From the phonon frequency calculations of solids, vibrational contribution of the thermodynamic function ( $F_{\mathrm{vib}}(T)$ ) can be calculated using a direct method. Direct method uses first-principles-based force constants to form up a dynamical matrix. The force constants are calculated from the Hellmann-Feynman forces induced by the displacement of individual atoms. In this formalism, dynamical matrix of a crystal is defined as,

$$D(k;\mu\nu) = \frac{1}{\sqrt{M_\mu M_\nu}} \sum_{\mathbf{m}} \Phi(0,\nu;\mathbf{m},\nu) e^{-2\pi i \mathbf{k}\left[\mathbf{R}(0,\mu) - \mathbf{R}(\mathbf{m},\nu)\right]} \qquad (4)$$

where $M_\mu$, $M_\nu$ and $\mathbf{R}(0,\mu)$, $\mathbf{R}(\mathbf{m},\nu)$ are masses and positions of atoms $\mu$ and $\nu$, respectively. The summation index $\mathbf{m}$ runs over all atoms of the crystal. $\mathbf{k}$ is the wave vector in the first Brillouin zone and $\Phi(0,\nu;\mathbf{m},\nu)$ is the force constant matrix which can be constructed from the induced Hellman-Feynman forces by atomic displacements. Phonon frequencies $\omega(\mathbf{k},j)$ and the polarization vector $\mathbf{e}(\mathbf{k},j)$ are given from the eigenvalues and the eigenvectors of the dynamical matrix:

$$\omega^2(\mathbf{k},j)\mathbf{e}(\mathbf{k},j) = D(\mathbf{k})\mathbf{e}(\mathbf{k},j) \qquad (5)$$

with the index $j$ for the normal modes. With this, total phonon density of states can be evaluated from $\omega(\mathbf{k},j)$ and $\mathbf{e}(\mathbf{k},j)$ as,

$$g(\omega) = \frac{1}{nd\Delta\omega} \sum_{\mathbf{k},j} \delta_{\Delta\omega}\left[\omega - \omega(\mathbf{k},j)\right] \qquad (6)$$

where $n$ is the number of sampling wave vectors, $d$ is the dimension of the dynamical matrix, $\Delta\omega$ is the frequency interval, and the delta function $\delta_{\Delta\omega}$ is defined as

$$\delta_{\Delta\omega}(x) = \begin{cases} 1 & \text{if } -\frac{\Delta\omega}{2} < x < +\frac{\Delta\omega}{2} \\ 0 & \text{otherwise.} \end{cases} \qquad (7)$$

For a given phonon density of states, Sternik and Parlinski showed that the vibrational contribution of the free energy, $F_{\mathrm{vib}}(T)$, can be calculated within the harmonic approximation as,

$$F_{vib}(T) = rk_BT \int_0^{\infty} d\omega\, g(\omega) \ln\left[2\sinh\left(\frac{\hbar\omega}{2k_BT}\right)\right] \quad (8)$$

Using Eqns (2) and (8), free energies of solid MgO and $Mg(OH)_2$ crystals at constant temperature can be calculated solely based on first-principles methods.

Effect of doping on MgO hydroxylation

The fundamental question is, how can we improve the stability of the MgO layer? In this work, we applied the cationic doping concentration of 1 out of 16 Mg sites (6.25 at%Mg) for both MgO and $Mg(OH)_2$. For the doped $Mg(OH)_2$ crystals, 4×2×2 orthorhombic supercell with 16($Mg(OH)_2$) was built with one cationic doping site. Electronic energy, thermal energy, and entropy values for MgO and $Mg(OH)_2$ are all in close agreement with previous first-principles study by Duan and Sorescu. The calculated Gibbs free energy of hydroxylation (-26.5 kJ / mol) also agrees very well with the prediction from experimental database (-27.1 kJ / mol). The negative Gibbs free energy indicates that the oxide film degradation via hydroxylation occurs spontaneously. The results of the dissolution thermodynamics is summarized in Tables I and II.

**Table I** First-principles-calculated thermochemical properties of reactants and products from the overall hydroxide reaction shown in Eqn. (1). All units are in kJ / mol.

| $T$ = 298 K<br>$p$ = 1 bar | $U_{elec}$ | $F_{vib}(T)$ | $pV$ | $E_{rot}(T)$ | $G(T,p)$ |
|---|---|---|---|---|---|
| MgO (s) | -1156.1 | 10.82 | - | - | -1145.2 |
| $H_2O$ (g) | -1370.0 | 17.90 | 2.48 | 7.44 | -1352.1 |
| $Mg(OH)_2$ (s) | -2601.2 | 68.90 | - | - | -2532.3 |
| $\Delta_h G = G(Mg(OH)_2) - \left[G(MgO) + G(H_2O_{(g)}) + \delta G^{g\to l}_{H_2O}\right] = -26.5$ (kJ/mol) | | | | | |

In Table I, the first-principles calculated energy and entropy values for the oxide and the hydroxide crystals are shown for standard temperature and pressure condition (298 K, 1 bar). Electronic energy, thermal energy, and entropy values for MgO and $Mg(OH)_2$ are all in close agreement with previous first-principles studies. The calculated Gibbs free energy of hydroxylation at standard condition is -26.5 kJ / mol. This agrees very well with the prediction from the experimental database (-27.1 kJ / mol). The negative Gibbs free energy indicates that the oxide film degradation via hydroxylation occurs spontaneously. We also found that the thermodynamic driving force for the hydroxylation mostly attributes to the decrease in electronic energy ($\Delta_h U_{elec} < 0$) which compensates the increase in thermal energy ($\Delta_h F_{vib} > 0$).

Subsequently, we calculated hydroxylation free energies for the doped oxide and hydroxide crystals with six different types of cationic doping ($Zn^{2+}$, $Al^{3+}$, $Y^{3+}$, $Ce^{3+}$, $Ce^{4+}$, and $Zr^{4+}$). The results are summarized in Table II **Table** along with electronic ($\Delta_h U_{elec}$) and thermal ($\Delta_h F_{vib}$) contributions to $\Delta_h G$. When doped with cationic impurities, a clear trend was found for $\Delta_h G$ with respect to the charge state of the impurity atoms. While doping with isovalent $Zn^{2+}$ shows minimal impact, doping with higher charge state (3+ and 4+) elements leads to a significant increase in the hydroxylation free energy. For $Ce^{4+}$ and $Zr^{4+}$ doped oxides, the doping effect is significant enough to change the sign of $\Delta_h G$ from negative to positive. As a result, hydroxylation reaction becomes no longer spontaneous with the doping. The similar trend found in $\Delta_h U_{elec}$ suggests that such doping effect has the electronic origin. The trend is most apparent from a comparison between $Ce^{3+}$ doping and $Ce^{4+}$ doping, where significant difference between hydroxylation free energies (26.8 kJ / mol) can only attribute to the difference in their impurity charge state. The change in sign from a highly favorable reaction to unfavorable one is a potentially powerful information on use of doping in slowing down failure of MgO grains.

**Table II** First-principles calculated electronic, vibrational, and overall free energy changes during the hydroxylation of the doped MgO crystals.

| (298 K, 1 bar) | $\Delta_h U_{elec}$ (kJ/mol) | $\Delta_h F_{vib}$ (kJ/mol) | $\Delta_h G$ (kJ/mol) |
|---|---|---|---|
| Undoped | -75.2 | +40.2 | **-26.4** |
| $Zn^{2+}$-doped | -73.1 | +40.5 | **-24.0** |
| $Al^{3+}$-doped | -53.8 | +40.8 | **-4.5** |
| $Y^{3+}$-doped | -59.1 | +40.3 | **-10.2** |
| $Ce^{3+}$-doped | -61.1 | +41.0 | **-11.5** |
| $Ce^{4+}$-doped | -33.4 | +40.2 | **+15.3** |
| $Zr^{4+}$-doped | -31.1 | +40.6 | **+18.1** |

First-principles-assisted kinetic Monte Carlo (kMC) model

Let us examine first how similar information can be useful in understanding nanometer scale evolution of surface with doping elements such as Ce. The first model we are developing is for the alloy exposed to electrolyte without the MgO layer on the top. We will eventually describe the MgO grains and their hydrolysis. To analyze nanometer-scale corrosion of Mg surfaces, we employ lattice-based kinetic Monte Carlo (kMC) technique. While the dissolution parameters for Mg atoms on the surfaces that are in contact with aqueous solution will be set from experimental polarization curve of pure Mg, other parameters for atomistic diffusion process will be directly extracted from first-principles DFT calculations. For a given surface morphology and the alloying composition, the outcome of the simulation will provide the corrosion current density (*e.g.* dissolution rate) and the surface morphology of the alloy surface as a function of time. The model will also provide selective dissolution mechanism during the corrosion process and will give insights on the corrosion performance of a given alloying composition.

Simulation setup

In KMC simulation, atoms and molecules are modeled in a coarse-grained way which would represent averages of behaviors that arises from the transitions between different atomistic-scale configurations. We use lattice-based kMC module from SPPARKS code from Sandia National Laboratory to describe dissolution and diffusion of metal atoms at alloy surfaces. The same code will be used in future to describe grains.

For the lattice-based kMC simulation, we employ (100)-facing fcc structured slab surface model with lattice parameter of 4 Å. The 2D periodic surface unit cell is 8 nm × 8 nm wide (800 lattice sites per layer) and 34 atomic-layer thick. The rest of the 6 layers of atomic lattices are initially assigned as solution sites, *i.e.* non-occupied sites. The resulting slab is 6 nm thick with 27200 lattice sites that are initially occupied with Mg or RE atoms. At the beginning of simulation, metal sites are assigned by randomly distributing Mg and RE atoms with a given alloying composition, *i.e.* the doping concentration. Both upward and downward facing surfaces in the slab are exposed to the solution. During the simulation, only diffusion and dissolution steps are considered.

Dissolution model

Selective dissolution of Mg alloy surface is simulated by allowing only Mg atoms to dissolve from the surface while more cathodic RE element remains at the surface. For each Mg atom, propensity of its dissolution is determined by Arrhenius-type formula:

$$r_{\text{dissolution}} = \nu_{\text{diss}} \exp\left[-\left(E_{\text{diss}}(n) - \phi\right)/\text{kT}\right] \tag{9}$$

where $r_{\text{dissolution}}$ is dissolution rate, $\nu_{\text{diss}}$ is frequency for the dissolution process, $\phi$ is overpotential, and $E_{\text{diss}}$ is dissolution barrier for each Mg atom as function of number of nearest occupied sites $n$. We employed the frequency value of $\nu_{\text{diss}} = 10^4$ $\text{sec}^{-1}$ from the similar kMC studies.

Diffusion model

Diffusion of Mg and RE atoms at the surface is modeled with hopping mechanism between the nearest-neighbor sites. Instead of using the conventional bond-breaking scheme for diffusion model, we use site-energy model in which final state atomic configuration as well as initial state atomic configuration is taken into account. In site-energy model, diffusion barrier is the sum of site-dependent energy $E_{\text{site}}(n)$ and the constant diffusion barrier $E^0_{\text{diff}}$. The interaction energy between Mg and RE atoms ($E^{\text{Mg-RE}}$) could also affect the diffusion barrier. The resulting expression for the rate of diffusion is as follows:

$$r_{\text{diffusion}} = \nu_{\text{diff}} \exp\left[-\left(E_{\text{site}}(n) + E^0_{\text{diff}} + E^{\text{Mg-RE}}\right)/\text{kT}\right] \tag{10}$$

We set $\nu_{\text{diff}} = 10^{13}$ $\text{sec}^{-1}$ based on the Debye frequency of solid magnesium at room temperature (~ $1.2 \times 10^{13}$ $\text{sec}^{-1}$). The site-dependent energy and the diffusion barrier will be determined by performing first-principles DFT calculations of Mg structures embedded with vacancies, surfaces, islands, and clusters.

Selective dissolution of RE-doped Mg surface

As preliminary analysis, we performed KMC simulation on the selective dissolution of 10 at% Ce-doped Mg surface. Based on first-principles transition-state calculation of surface vacancy diffusion and surface ad-atom diffusion on Mg (100) surface, we obtained the average diffusion barrier of 0.40 eV for hopping Mg atoms between the same atomic configurations. For Ce atoms, slightly higher diffusion barrier of 0.50 eV was applied. For both types of atoms, 0.25 eV of cohesive energy per bonding was applied for each occupied nearest neighbor site to assign the site-dependent energies. Diffusion barrier for Mg atoms was assumed to be the same as the diffusion barrier at the surface. To reflect the segregation of RE elements within the alloy matrix, a repulsive interaction potential of 0.05 eV / site was set between Mg and Ce atoms.

Figure illustrates the doping effect on the dissolution of alloy surfaces by plotting the surface current density and the surface composition for the first 50 *ms* of selective dissolution with a given overpotential of -0.3 *V*. First, increase of the dissolution rate becomes noticeably slower with the Ce doping when compared with pure Mg dissolution. It is also found that the surface composition of Mg gradually decreases from its bulk composition (90 *at%*) and converges to a much lower concentration (~75 *at%*). This indicates that the selective dissolution of Mg atoms leads to a surface segregation of Ce atoms near surface so that it would slow down the Mg dissolution. Nanometer-scale evolution of 10 *at%* Ce-doped Mg surface depicted in Figure confirms this argument. The figure clearly shows that the selective dissolution of Mg leads to higher concentration of segregated Ce clusters at the surface.

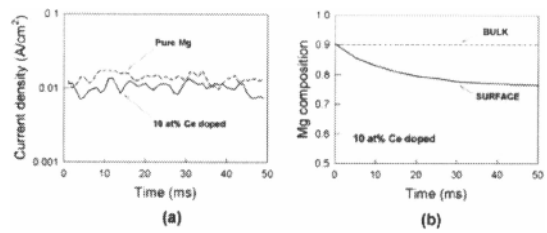


Figure 3. (a) Dissolution rate (in the unit of current density) of pure and 10 at% Ce-doped Mg surfaces, and (b) surface Mg composition of the Ce-doped surface. Dashed line in (b) indicates the bulk Mg composition of the alloy (10 at%). Both graphs are plotted for the first 50 ms of KMC simulation.

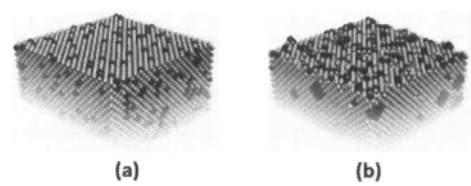


Figure 4. Snapshot from the dissolution of 10 at% Ce-doped Mg surface (8nm × 8nm) at (a) t = 0 ms and (b) t = 50 ms. Grey spheres represent Mg atoms and black spheres represent Ce atoms.

Before we describe the larger length-scale beyond kMC, it shows that elemental design of surfaces and understanding the fundamental science aspects of failure of MgO surface layer is critical for better design of alloy phase. In addition, we have results from reactive surfaces that are treated using coupled electrochemical models using computational fluid dynamics (CFD), both negative differential effect and effects of RE doping is currently being implemented in the microscale models. Long-term goal of our research is to improve the description of failure of grains and dissolution mechanics by coupling DFT-kMC and CFD methods.

Fluid-dynamics Simulation of Corrosion at a Pit

The calculated thermodynamic quantities from DFT can be fed into FEM model by resorting to an information integration method described in this section. Rate constants for chemical and

electrochemical reactions can be calculated from Gibbs free energy of activation by:

$$k = \frac{k_B T}{h} \exp\left(-\frac{\Delta G^*}{RT}\right) \tag{11}$$

where $k_B$ is Boltzmann's constant and $h$ is Planck's constant. The surface coverage of reactive species ($\theta_j$) in electrochemical reactions can be related to the solution chemistry using a Langmuir model [4]:

$$\theta_j = \frac{r_j a_j}{1 + \sum_k r_k a_k} \tag{12}$$

$$r_j = \frac{k_B T}{h} \exp\left(-\frac{\Delta G_{ads,j}}{RT}\right) \tag{13}$$

where $a_j$ is the activity of the $j$-th reactive species at the metal surface and the coefficient $r_j$ is a scaled adsorption constant. Conventionally, both anodic metal dissolution and cathodic reduction reactions are assumed to follow an empirical Tafel's law and the parameters in Tafel's equation are fitted from experimental data or from first-principles calculated kinetics with corrections for potential. In this work, the general form of current density is:

$$i = i_a + i_c \tag{14}$$

$$i_a = \sum_k \sum_j n_m^k F k_{a,j}^k \left(\theta_{j,s}^k\right)^{m_j^k} \exp\left(\frac{\alpha_{a,j}^k n_m^k F(\psi - \phi)}{RT}\right) \tag{15}$$

$$i_c = -\sum_j n_j F k_{c,j} \left(\theta_{o,s}\right)^{p_j} \exp\left(-\frac{\alpha_{c,j} n_j F(\psi - \phi)}{RT}\right) \tag{16}$$

In this way, anodic and cathodic current densities are quantitatively correlated to the applied potential ($\psi$), electrostatic potential in the solution ($\phi$), temperature ($T$), and most importantly, the material and solution chemistry, which can be reflected by the reaction rate constant ($k$) and surface coverage of reactants ($\theta$). Note that the subscript $j$ represents the $j$-th aggressive ion in Eq. (15) and the $j$-th reduction reaction in Eq. (16). It is widely recognized that the negative difference effect (NDE) is a critical phenomenon in magnesium corrosion. Evolution of gas bubbles from a pit can perturb ion diffusion, and hence the growth of a pit. In order to quantitatively characterize such phenomenon, $H_2$ gas bubble generation as well as bubble redistribution due to multi-phase flow need to be fully taken into consideration. Figure 5 gives $H_2$ bubble distribution in systems with different electrolyte flow rates. Electrochemical and chemical reactions involved in this system were assumed to be the same as those in pure Mg corrosion.

$$Mg \rightarrow \equiv Mg^+ + e^- \qquad \text{and } Mg^+ \rightarrow Mg^{2+} + e^-$$

$$Mg^+ + H_2O \rightarrow Mg^{2+} + OH^- + 0.5H_2 \text{ and } 2H^+ + 2e^- \rightarrow H_2$$

$$Mg^{2+} + 2OH^- \rightarrow Mg(OH)_2 \text{ and } MgO + H_2O \rightarrow Mg(OH)_2$$

In a stagnant electrolyte system (Figure 5a), gas bubbles arise along the peripheral lip of the pit, which was confirmed in experiments. As we increased the flow speed, the volume fraction of gas bubbles was reduced and the most prominent volume fraction appeared on one side of the pit surface facing towards the flow direction (see figure 5b). The NDE phenomenon was clearly identified (see figure 5d), where the hydrogen evolution rate increased rather than decreased with increasing potential. We have also developed a detailed pit growth and propagation model in the CFD scale using surface dissolution equations for intermetallic particles around Al-2024 alloy using a similar approach. [2, 5]

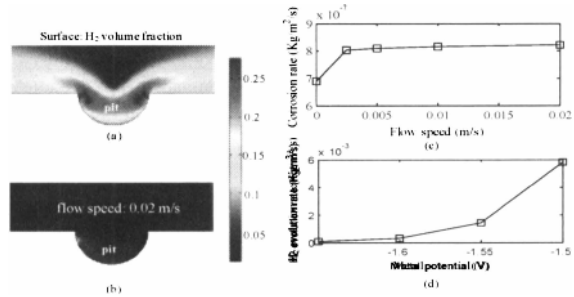


Figure 5. The effect of multiphase flow on corrosion: (a) $H_2$ bubble volume fraction in a stagnant system, (b) $H_2$ bubble volume fraction in a flowing system, (c) corrosion rate as a function of flow speed, and (d) $H_2$ evolution rate

In conclusion, robust mesoscale model of grain structure and incorporation of intermetallic phase across the length scale will be required for more realistic simulations that allow us to explore the effects of doping and alloy composition in a more comprehensive fashion. Such model will therefore be used to quantify the effect of microstructure and chemical environment in determining failure of surface film and the subsequent metal loss from damaged surface or pits.

**Acknowledgments**

Research was sponsored in part by the Army Research Laboratory and was accomplished under Cooperative Agreement Number W911NF-10-2-0112. The views and conclusions contained in this document are those of the authors and should not be interpreted as representing the official policies, either expressed or implied, of the Army Research Laboratory or the U.S. Government. The U.S. Government is authorized to reproduce and distribute reprints for Government purposes notwithstanding any copyright notation herein. The rest of the funding is from the Office of Naval Research grant #s N00014-04-1-0688 and N00014-06-1-0315.

**References**

1. H. Kwak and S Chaudhuri; "Cationic doping of MgO surfaces to build corrosion protection in Mg alloys." *Journal of Alloys and Compounds* 509, 32 (2011) 8189-8198.
2. J. Xiao, H. Kwak, S. Chaudhuri, "Understanding the Role of Intermetallic Particles in Localized Corrosion" *Proceedings of MS&T 2011, Columbus, OH*; 2011; p1374-1385.
3. H. Kwak, J. Xiao, S. Chaudhuri, "First-Principles-Based Analysis on the Role of Rare-earth Doping on Mg Alloy Corrosion" *Proceedings of MS&T 2011, Columbus, OH*; (2011) 1386-1396
4. A. Anderko, N. Sridhar, D.S. Dunn, A General Model for the Repassivation Potential as a Function of Multiple Aqueous Solution Species, *Corrosion Science*, 46(2004) 1583-1612
5. J. Xiao, S. Chaudhuri; "Predictive modeling of localized corrosion: An application to aluminum alloys"; *Electrochim Acta* 56, 16(2011), 5630-5641